This article has been accepted for publication in a future issue of this journal, but has not been fully edited. Content may change prior to final publication. Citation information: DOI 10.1109/TIE.2017.2674589, IEEE Transactions on Industrial Electronics

Revisited Perturbation Frequency Design Guideline for Direct Fixed-Step Maximum Power Point Tracking Algorithms

Jyri Kivimäki, *Student Member, IEEE*, Sergei Kolesnik, *Student Member, IEEE*, Moshe Sitbon, *Student Member, IEEE*, Teuvo Suntio, *Senior Member, IEEE*, and Alon Kuperman, *Senior Member, IEEE*

***Abstract*—In order to optimize the performance of direct (or perturbative) fixed-step maximum power point tracking algorithms (e.g. perturb & observe and incremental conductance), two design parameters – perturbation frequency and step size – must be selected. The main requirement for perturbation frequency design is ensuring the period between two successive perturbations is longer than settling time of photovoltaic generator power transient. According to existing design guidelines, perturbation frequency should be selected at maximum power point, corresponding to standard test conditions. However, due to finite resolution of digital controllers, maximum power region rather than single maximum power point exists in practice. Therefore, operating point can arbitrarily reside within this region, belonging either to constant-current or constant-voltage I-V curve parts. It is shown that photovoltaic generator power transient settling process is significantly slower in constant current than maximum power region due to increased value of dynamic resistance. Consequently, perturbation frequency design should be carried out in constant-current region rather than at maximum power point. Short-circuit condition should be selected as worst-case design operation point, where photovoltaic generator dynamic resistance obtains highest value. Then, perturbation frequency design becomes photovoltaic generator independent, influenced only by interfacing converter component values. Experimental results validate presented findings successfully.**

***Index Terms*—Photovoltaic generators, maximum power point tracking, perturbation frequency.**

Manuscript received July 10, 2016; revised October 24, 2016 and December 04, 2016; accepted December 07, 2016.

J. Kivimäki and T. Suntio are with the Dept. of Electrical Engineering, Tampere University of Technology, Tampere FI-33101, Finland (emails: jyri.kivimaki@tut.fi, teuvo.suntio@tut.fi).

S. Kolesnik and M. Sitbon are with the Dept. of Electrical Engineering and Electronics, Ariel University, Ariel 40700, Israel (emails: skolesnik@gmail.com, sitbon222@gmail.com).

A. Kuperman is with the Dept. of Electrical and Computer Engineering, Ben-Gurion University, Beer-Sheva 8410501, Israel and also with the Dept. of Electrical Engineering and Electronics, Ariel University, Ariel 40700, Israel (email: alonk@bgu.ac.il)

I. Introduction

PHOTOVOLTAIC generators (PVG) are operated in solar energy conversion systems either at maximum power point (MPP) [1-4] to extract as much energy as possible or at limited power point (LPP) to prevent interfacing converter load overvoltage [5-8]. As for today, the most popular MPP tracking (MPPT) methods are fixed step perturb and observe (P&O) [25] and incremental conductance [26] algorithms, belonging to the class of direct MPPT techniques [21]. There, a small perturbation Δx is injected into the system every ΔT seconds and after a transient, lasting T_Δ seconds, corresponding change in PVG power $p[k] - p[k\text{-}1]$ is observed (cf. Fig .1) for determining its polarity and subsequent driving the operation point towards the MPP [1]. In this respect, two design parameters are perturbation frequency (i.e. the reciprocal of time interval ΔT between two consecutive perturbation instants) and perturbation step size Δx. As revealed in [2] and [21], while the maximum perturbation frequency should be limited by settling time of the PVG power transient induced by the injected perturbation (i.e. $\Delta T > T_\Delta$ must hold for every operating point), minimum perturbation step size depends on the maximum expected irradiation variation rate.

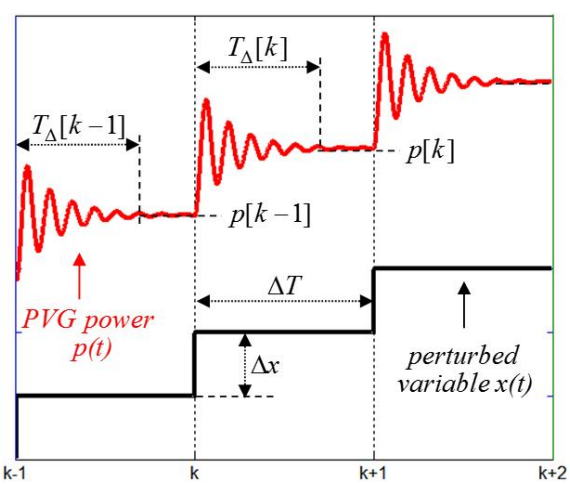

Fig. 1. Perturb & observe MPPT method short-time dynamics.

It was shown that regardless of perturbation step size Δx, a stable three-point behavior is ensured if the time interval ΔT is properly selected. If a too small ΔT is selected, the P&O algorithm can be confused and the operating point may

0278-0046 (c) 2016 IEEE. Personal use is permitted, but republication/redistribution requires IEEE permission. See http://www.ieee.org/publications_standards/publications/rights/index.html for more information.

This article has been accepted for publication in a future issue of this journal, but has not been fully edited. Content may change prior to final publication. Citation information: DOI 10.1109/TIE.2017.2674589, IEEE Transactions on Industrial Electronics

become unstable, entering disordered or chaotic behaviors. On the other hand, selecting a too big ΔT penalizes MPPT speed and efficiency.

Due to the highly nonlinear PVG nature and widely varying environmental conditions (irradiance and ambient temperature), the validity of selected design parameters at each possible operation point has to be properly verified [11]. The PGV I-V curve (cf. Fig. 2) theoretically contains two distinct regions separated by the MPP: constant current region (CCR) for voltages lower than MPP voltage, and constant voltage region (CVR) for voltages higher the MPP voltage (the categorization is based on the variable, which stays practically constant within the named region [9-13]). The low-frequency PVG dynamic resistance r_{pv} plays the role of respective characteristic resistance, behaving as shown in Fig. 2 [14]. Nevertheless, due to finite resolution of digital controllers based systems, it is impossible in practice to locate the MPP exactly. Moreover, perturb & observe based systems are known to oscillate between three operating points around the MPP in steady state. Therefore, a maximum power region is actually formed at the vicinity of MPP, referred thereafter as constant-power region (CPR), as shown in Fig. 2. It is interesting to note that the existence of the CPR is utilized in ripple correlation control MPPT algorithm [12].

In case single-loop MPPT control structure is employed (i.e. the MPPT algorithm directly calculates the PVG interfacing power converter (IPC) duty cycle, as shown in Fig. 3), MPPT perturbation frequency is recommended to be designed at the MPP corresponding to standard operation conditions (STC with irradiance of 1000W/m^2 and 25°C temperature). Note that the data regarding this point is usually provided by PVG manufacturer. Moreover, the value of r_{pv} at MPP (required in perturbation frequency calculation as shown next) equals the value of corresponding static resistance [14] and may be easily calculated from the datasheet.

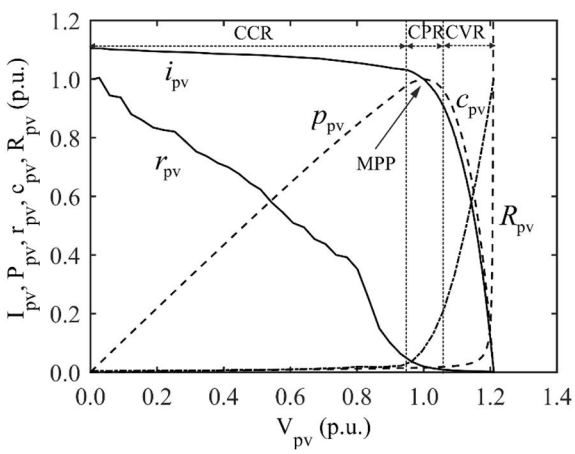

Fig. 2. Normalized behavior of PVG current I_{pv}, power P_{pv}, dynamic resistance r_{pv}, dynamic capacitance c_{pv} and static resistance R_{pv} as function of PVG voltage. Currents and voltages are normalized according to respective PVG MPP values while resistances and capacitance are normalized according to their peak values.

It is well known that PVG dynamic resistance r_{pv} affects the dynamic behavior of the combined solar energy conversion system [10], [22]. In case of a single-loop MPPT control structure, it mainly affects the damping and hence transient settling time [15], [23]. According to Fig. 2, damping is reduced when the operating point moves to the CCR due to dynamic resistance rise, i.e. settling time of PVG power transient increases as well and would hence be longest at the short-circuit condition. Thus, in case the operating point is expected to occasionally reside in the CCR, perturbation frequency design guidelines must take this into account, even though selecting higher ΔT results in slower tracking speed and reduced efficiency. When the operating point moves from CPR to CCR, dynamic resistance rapidly increases (cf. Fig. 2), justifying reconsideration of perturbation frequency design guidelines, presented in [2], [21], stating that the latter should be designed at STC MPP. It should be emphasized that perturbation step size design guidelines given in [2], [21] remain valid and are utilized in this paper. Scientific contributions of this work may thus be summarized as follows:

- Justification of the CPR existence is explicitly provided.
- It is shown that the operating point can move from CPR to CCR even during steady-state MPPT operation, leading to longer PVG power transient settling time than the one expected at MPP.
- Revisited perturbation frequency design guidelines are provided.
- It is shown that it is possible to disregard the PVG during perturbation frequency design process at the expense of slightly reduced MPPT bandwidth.

It should be mentioned that perturbation period much lower than the settling time of the system response has been recently adopted in [35, 36]. Since it is not necessary to wait for the system to reach a steady state after each MPPT perturbation, higher efficiency and faster response to irradiance changes may be achieved. By contrast, the steady-state oscillation for the higher perturbation frequency is larger than that for the lower perturbation frequency due to the confusion caused by noise. Even though only experimental investigation was conducted without solid analytical background, this is undoubtedly a very interesting and promising future research direction.

The rest of the paper is organized as follows. Open-loop small-signal dynamics of the combined PVG-IPC system is developed in Section II. Section III reveals the revisited design rules of perturbation frequency. Experimental validation of the proposed technique is presented in Section IV followed by conclusions drawn in Section V.

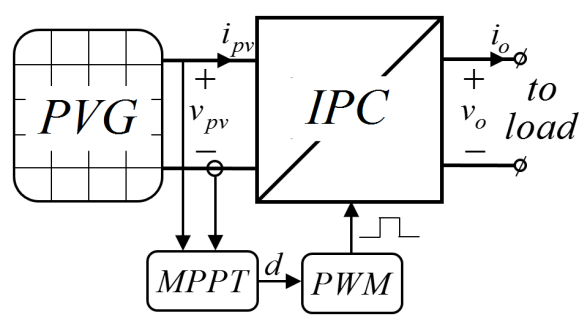

Fig. 3. Single loop MPPT control structure.

0278-0046 (c) 2016 IEEE. Personal use is permitted, but republication/redistribution requires IEEE permission. See http://www.ieee.org/publications_standards/publications/rights/index.html for more information.

This article has been accepted for publication in a future issue of this journal, but has not been fully edited. Content may change prior to final publication. Citation information: DOI 10.1109/TIE.2017.2674589, IEEE Transactions on Industrial Electronics

II. COMBINED SYSTEM DYNAMICS

Refer to the general representation of a solar energy conversion system shown in Fig. 3, where power grid, grid-connected inverter or storage battery typically serve as load.

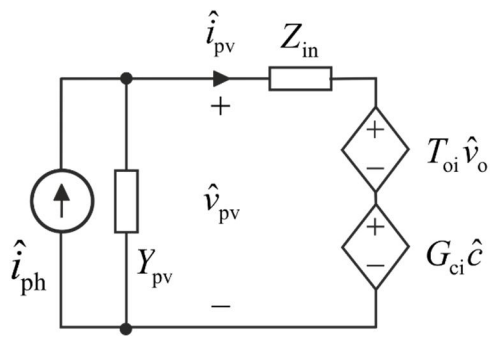

Fig. 4. Open-loop PVG-side small-signal equivalent circuit of a solar energy conversion system.

Fig. 4 presents the corresponding open-loop PVG-side small-signal equivalent circuit consisting of PVG Norton equivalent (i_{ph}, $Y_{pv} = 1/r_{pv}$) [24] and IPC input stage with

$$1/r_{pv} = -\frac{\partial i_{pv}}{\partial v_{pv}} \tag{1}$$

and

$$\begin{aligned} \hat{v}_{pv} &= \frac{Z_{in}}{1+Z_{in}Y_{pv}}\hat{i}_{ph} + \frac{T_{oi}}{1+Z_{in}Y_{pv}}\hat{v}_o + \frac{G_{ci}}{1+Z_{in}Y_{pv}}\hat{c} \\ \hat{i}_{pv} &= \frac{1}{1+Z_{in}Y_{pv}}\hat{i}_{ph} - \frac{Y_{pv}T_{oi}}{1+Z_{in}Y_{pv}}\hat{v}_o - \frac{Y_{pv}G_{ci}}{1+Z_{in}Y_{pv}}\hat{c}, \end{aligned} \tag{2}$$

where $\hat{c}$ denotes the general control variable (duty cycle in case of single-loop MPPT control structure);G_{ci}, T_{oi} and Z_{in} denote the IPC control-to-input-voltage transfer function, output-to-input voltage transfer function and input impedance, respectively. It is known that temperature significantly affects the PVG power but its dynamics is quite slow due to the large thermal capacity of the photovoltaic modules, as assumed in [2]. Therefore, temperature effect is disregarded in (2) as well. The control-to-PVG-voltage transfer function in (2) is of particular interest for perturbation frequency design. Decomposing PVG variables into DC and small-signal parts $P_{pv} + \hat{p}_{pv} = (V_{pv} + \hat{v}_{pv})(I_{pv} + \hat{i}_{pv})$, small signal PVG power can be obtained as [2]

$$\hat{p}_{pv} = I_{pv}\hat{v}_{pv} + V_{pv}\hat{i}_{pv} + \hat{i}_{pv}\hat{v}_{pv}. \tag{3}$$

Defining static resistance as

$$R_{pv} = \frac{V_{pv}}{I_{pv}} \tag{4}$$

while rearranging (1) as [10]

$$\hat{i}_{pv} \approx -\frac{1}{r_{pv}}\hat{v}_{pv}, \tag{5}$$

eq. (3) is further reformulated as

$$\hat{p}_{pv} \approx V_{pv}\left(\frac{1}{R_{pv}} - \frac{1}{r_{pv}}\right)\hat{v}_{pv} - \frac{1}{r_{pv}}\hat{v}_{pv}^2. \tag{6}$$

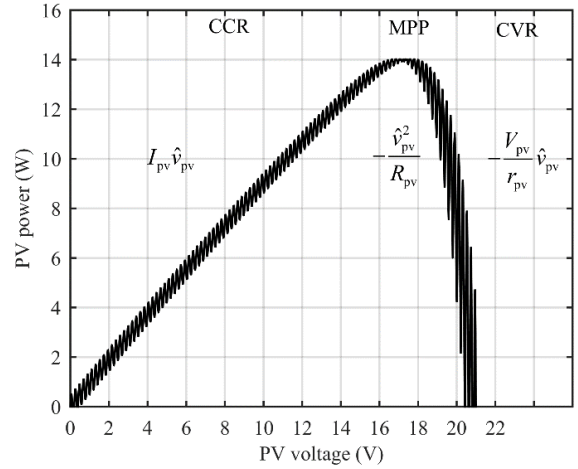

(a) P-V curve.

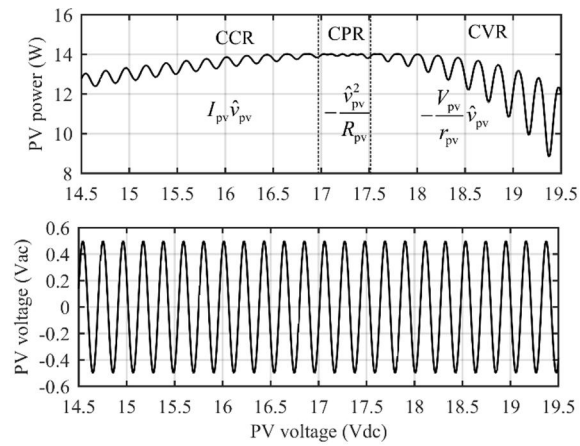

(b) zoom around CPR.

Fig. 5. Raloss SR30-36 PV panel voltage induced power ripple.

According to (6), small-signal behavior of PVG power is dictated by (assuming $\hat{v}_{pv} << V_{pv}$ **)**

- $\hat{p}_{pv} \approx I_{pv}\hat{v}_{pv}$ in CCR ($r_{pv} >> R_{pv}$ in this region);
- $\hat{p}_{pv} \approx -\frac{V_{pv}}{r_{pv}}\hat{v}_{pv} = V_{pv}\hat{i}_{pv}$ in CVR (here, $r_{pv} << R_{pv}$);
- $\hat{p}_{pv} \approx -\frac{1}{R_{pv}}\hat{v}_{pv}^2$ in CPR ($R_{pv} \approx r_{pv}$ at the vicinity of MPP).

Fig. 5 demonstrates the effect of perturbing terminal voltage of Raloss SR30-36 photovoltaic (PV) panel [13] on its power. Fig. 5a presents the P-V curve upon voltage operation point sweep from short-circuit to open-circuit conditions. The PVG power ripple performance clearly follows the small-signal behavior given above: in CCR, $\hat{p}_{pv}$ is nearly constant (since I_{pv} is practically constant) and in phase with the PVG voltage ripple $\hat{v}_{pv}$; in CVR, $\hat{p}_{pv}$ increases along with the PVG voltage DC operation point V_{pv} and is in opposite phase to the PVG voltage ripple $\hat{v}_{pv}$; in CPR, $\hat{p}_{pv}$ is close to zero. Fig. 5b presents the power ripple behavior zoomed around CPR, clearly demonstrating both CPR existence and near-zero power ripple amplitude. As discussed in the Introduction, the

0278-0046 (c) 2016 IEEE. Personal use is permitted, but republication/redistribution requires IEEE permission. See http://www.ieee.org/publications_standards/publications/rights/index.html for more information.

This article has been accepted for publication in a future issue of this journal, but has not been fully edited. Content may change prior to final publication. Citation information: DOI 10.1109/TIE.2017.2674589, IEEE Transactions on Industrial Electronics

operating point may reside in any of the three mentioned regions even during steady-state MPPT operation.

III. PVG POWER TRANSIENT BEHAVIOR

According to [21] and [37], when PVG is connected to an IPC, the control-to-input-voltage transfer function of the combined system is given by (cf. (2))

$$G_{\mathrm{ci}}^{\mathrm{pv}}(s)=\frac{G_{\mathrm{ci}}}{1+Z_{\mathrm{in}}Y_{\mathrm{pv}}}=-V_{\mathrm{DC}}\frac{\omega_{\mathrm{n}}^{2}\left(1+s/\omega_{\text{z-esr}}\right)}{s^{2}+2\zeta_{\mathrm{pv}}\omega_{\mathrm{n}}s+\omega_{\mathrm{n}}^{2}}. \tag{7}$$

It is important to emphasize that while the parameters values in (7) are IPC topology dependent, the structure of the control-to-input-voltage transfer function is IPC topology independent. For a small-signal duty cycle perturbation given by

$$\hat{d}(s)=\frac{\Delta D}{s}, \tag{8}$$

corresponding Laplace-domain PVG voltage response is

$$\hat{v}_{\mathrm{pv}}(s)=\hat{d}\cdot G_{\mathrm{ci}}^{\mathrm{pv}}=-V_{\mathrm{DC}}\Delta D\left(\frac{1}{s}-\frac{s+2\zeta_{\mathrm{pv}}\omega_{\mathrm{n}}-\dfrac{\omega_{\mathrm{n}}^{2}}{\omega_{\text{z-esr}}}}{s^{2}+s2\zeta_{\mathrm{pv}}\omega_{\mathrm{n}}+\omega_{\mathrm{n}}^{2}}\right). \tag{9}$$

Hence, in time domain there is

$$\hat{v}_{\mathrm{pv}}(t)=V_{\mathrm{DC}}\Delta D\left(\begin{array}{l}1-\dfrac{\sqrt{1+\dfrac{\omega_{\mathrm{n}}}{\omega_{\text{z-esr}}}\left[\dfrac{\omega_{\mathrm{n}}}{\omega_{\text{z-esr}}}-2\zeta_{\mathrm{pv}}\right]}}{\sqrt{1-\zeta_{\mathrm{pv}}^{2}}}\exp(-\zeta_{\mathrm{pv}}\omega_{\mathrm{n}}t)\\ \times\sin\left[\omega_{\mathrm{d}}t+\tan^{-1}\left\{\dfrac{\sqrt{1-\zeta_{\mathrm{pv}}^{2}}}{\zeta_{\mathrm{pv}}-\dfrac{\omega_{\mathrm{n}}}{\omega_{\text{z-esr}}}}\right\}\right]\end{array}\right) \tag{10}$$

with $\omega_{\mathrm{d}}=\omega_{\mathrm{n}}\sqrt{1-\zeta_{\mathrm{pv}}^{2}}$ and $0<\zeta_{\mathrm{pv}}<1$. Moreover, frequency of the capacitor ESR induced zero $\omega_{\text{z-esr}}$ is typically much higher than the natural frequency ω_{n}, further simplifying (13) into

$$\hat{v}_{\mathrm{pv}}(t)\approx V_{\mathrm{DC}}\Delta D\left(1-\frac{1}{\sqrt{1-\zeta_{\mathrm{pv}}^{2}}}\exp(-\zeta_{\mathrm{pv}}\omega_{\mathrm{n}}t)\sin\theta(t)\right) \tag{11}$$

with $\theta(t)=\omega_{\mathrm{d}}t+\tan^{-1}\left\{\dfrac{\sqrt{1-\zeta_{\mathrm{pv}}^{2}}}{\zeta_{\mathrm{pv}}}\right\}$. Therefore, utilizing (11) and (6), small-signal behavior of PVG power is dictated by

$$\hat{p}_{\mathrm{pv}}\approx-\Delta P_{\mathrm{pv}}^{CCR}\left(1\pm\frac{1}{\sqrt{1-\zeta_{\mathrm{pv}}^{2}}}\exp(-\zeta_{\mathrm{pv}}\omega_{\mathrm{n}}t)\cdot\sin\theta(t)\right) \tag{12a}$$

in CCR with $\Delta P_{\mathrm{pv}}^{CCR}=I_{\mathrm{pv}}V_{\mathrm{DC}}\Delta D$,

$$\hat{p}_{\mathrm{pv}}\approx-\Delta P_{\text{pv-ss}}^{CVR}\left(1\pm\frac{1}{\sqrt{1-\zeta_{\mathrm{pv}}^{2}}}\exp(-\zeta_{\mathrm{pv}}\omega_{\mathrm{n}}t)\cdot\sin\theta(t)\right) \tag{12b}$$

in CVR with $\Delta P_{\mathrm{pv}}^{CVR}=\dfrac{V_{\mathrm{pv}}V_{\mathrm{DC}}\Delta D}{r_{\mathrm{pv}}}$ and

$$\begin{aligned}\hat{p}_{\mathrm{pv}}&\approx-\Delta P_{\mathrm{pv}}^{CPR}\left(1-\frac{1}{\sqrt{1-\zeta_{\mathrm{pv}}^{2}}}\exp(-\zeta_{\mathrm{pv}}\omega_{\mathrm{n}}t)\cdot\sin\theta(t)\right)^{2}\\&=-\Delta P_{\mathrm{pv}}^{CPR}\left(\begin{array}{l}1-2\dfrac{1}{\sqrt{1-\zeta_{\mathrm{pv}}^{2}}}\exp(-\zeta_{\mathrm{pv}}\omega_{\mathrm{n}}t)\cdot\sin\theta+\\+\dfrac{1}{2\left(1-\zeta_{\mathrm{pv}}^{2}\right)}\exp(-2\zeta_{\mathrm{pv}}\omega_{\mathrm{n}}t)\left(1-\cos2\theta(t)\right)\end{array}\right)\end{aligned} \tag{12c}$$

in CPR with $\Delta P_{\mathrm{pv}}^{CPR}=\left(V_{\mathrm{DC}}\Delta D\right)^{2}/R_{\mathrm{pv}}$. Both corresponding steady-state PVG power variations and transient behaviors are well-evident from (12). It may be concluded that power transient settling time is dictated by corresponding envelope behavior, given by

$$env(\hat{p}_{\mathrm{pv}})=-\Delta P_{\mathrm{pv}}^{CCR}\left(1\pm\frac{1}{\sqrt{1-\zeta_{\mathrm{pv}}^{2}}}\exp(-\zeta_{\mathrm{pv}}\omega_{\mathrm{n}}t)\right) \tag{13a}$$

in CCR,

$$env(\hat{p}_{\mathrm{pv}})=-\Delta P_{\text{pv-ss}}^{CVR}\left(1\pm\frac{1}{\sqrt{1-\zeta_{\mathrm{pv}}^{2}}}\exp(-\zeta_{\mathrm{pv}}\omega_{\mathrm{n}}t)\right) \tag{13b}$$

in CVR and

$$env(\hat{p}_{\mathrm{pv}})\approx-\Delta P_{\mathrm{pv}}^{CPR}\left(\begin{array}{l}1\pm2\dfrac{1}{\sqrt{1-\zeta_{\mathrm{pv}}^{2}}}\exp(-\zeta_{\mathrm{pv}}\omega_{\mathrm{n}}t)\\+\dfrac{1}{1-\zeta_{\mathrm{pv}}^{2}}\exp(-2\zeta_{\mathrm{pv}}\omega_{\mathrm{n}}t)\end{array}\right) \tag{13c}$$

in CPR. Corresponding settling times T_{Δ} of (13) are obtained by solving

$$env(\hat{p}_{\mathrm{pv}})\big|_{t=T_{\Delta}}=-\Delta P_{\mathrm{pv}}\left(1\pm\Delta\right) \tag{14}$$

(with $0<\Delta<1$ denoting the relative magnitude of settling band) as

$$T_{\Delta}=-\frac{1}{\zeta_{\mathrm{pv}}\omega_{\mathrm{n}}}\ln\left(\Delta\sqrt{1-\zeta_{\mathrm{pv}}^{2}}\right) \tag{15a}$$

in CCR and CVR and

$$T_{\Delta}\approx-\frac{1}{\zeta_{\mathrm{pv}}\omega_{\mathrm{n}}}\ln\left(\frac{\Delta}{2}\sqrt{1-\zeta_{\mathrm{pv}}^{2}}\right) \tag{15b}$$

in CPR. It should be emphasized that since ζ_{pv} depends on r_{pv}, settling times must be evaluated separately for each region, taking into account appropriate values of PVG dynamic resistance, derived next.

IV. PVG DYNAMIC RESISTANCE

Consider a generalized PVG equivalent circuit, shown in Fig. 6(a), consisting of [27]:

- photocurrent source i_P;
- nonlinear current source i_D, usually modeled by one or more semiconductor diodes connected in parallel, drawing current attaining general form of

0278-0046 (c) 2016 IEEE. Personal use is permitted, but republication/redistribution requires IEEE permission. See http://www.ieee.org/publications_standards/publications/rights/index.html for more information.

This article has been accepted for publication in a future issue of this journal, but has not been fully edited. Content may change prior to final publication. Citation information: DOI 10.1109/TIE.2017.2674589, IEEE Transactions on Industrial Electronics

$$i_D = \sum_k I_{0k}\left(\exp\left\{\frac{v_{PV} - r_S i_{PV}}{\alpha_k V_T}\right\} - 1\right) \tag{16}$$

with I_{0k}, α_k and V_T denoting reverse saturation current, ideality factor of k-th diode and thermal voltage, respectively;

- equivalent shunt capacitance c_{PV};
- equivalent shunt and series resistances r_{SH} and r_S, respectively.

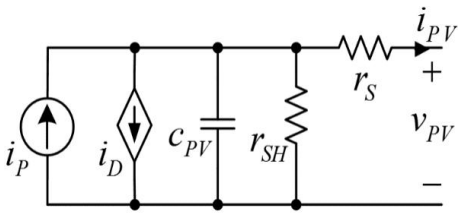

(a) Detailed.

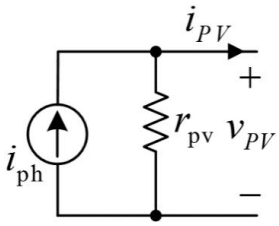

(b) Norton.

Fig. 6. PVG equivalent circuit.

PVG equivalent capacitance c_{PV} is typically offset by IPC input capacitance (e.g. C_2, cf. Fig. 7) and may be neglected. Equivalent circuit components possess the following environmental variables dependences: i_P is both irradiation and temperature dependent; i_D is temperature dependent; r_{SH} is irradiation dependent (yet often considered as constant) and r_S is constant. All the equivalent circuit parameters may be extracted utilizing manufacturer's datasheet data [28] – [30]. Consequently, PVG may be represented by dynamic Norton equivalent circuit shown in Fig. 6(b), where

$$r_{\text{pv}} = r_S + r_{SH} \parallel r_D, \quad i_{\text{ph}} = i_P \frac{r_{SH} \parallel r_D}{r_{\text{pv}}} \tag{17}$$

with r_D representing dynamic resistance of (16) [24]. Apparently, PVG dynamic resistance r_{pv} is both environmental variables and operating point dependent. Moreover, under the typical assumption of $k = 1$ in (16), it is obtained as [31]

$$r_{\text{pv}} = r_S + \frac{r_{SH}}{1 + W\left(\frac{I_0 r_{SH}}{aV_T}\exp\left(\frac{r_{SH}(i_P - I_0 - i_{PV})}{aV_T}\right)\right)} \tag{18}$$

with $W(\cdot)$ denothing the Lambert-W function. Behavior of PVG dynamic Norton parameters were recently investigated in [32]. Referring to (18), $i_P - I_0 - i_{PV} \approx 0$ at short circuit (SC) conditions and hence

$$r_{\text{pv}}\big|_{SC} \approx r_{SH} \tag{19}$$

since $W(x) << 1$ for $x << 1$ and $r_{SH} >> r_S$. At open circuit (OC) conditions, $i_{PV} = 0$ and hence

$$r_{\text{pv}}\big|_{OC} \approx r_S + \frac{r_{SH}}{W\left(\frac{I_0 r_{SH}}{aV_T}\exp\left(\frac{r_{SH}(i_P - I_0)}{aV_T}\right)\right)} \approx r_S \tag{20}$$

since $W(x) >> 1$ for $x >> 1$. It may then be concluded that the PVG dynamic resistance may approximately reside within $[r_S, r_{SH}]$ region of values. At the MPP, (18) is given by [33], [34]

$$r_{\text{pv}}\big|_{MPP} = \frac{aV_T(r_S + r_{SH})(w-1) - r_S r_{SH} i_P (1 - \frac{1}{w})}{r_{SH} i_P (1 - \frac{1}{w}) - aV_T(w-1)} \tag{21}$$

with $w = W\left(\frac{i_P e}{I_0}\right)$. Applying all the above assumptions to (21), it may be concluded that

$$r_{\text{pv}}\big|_{OC} < r_{\text{pv}}\big|_{MPP} \approx r_{SH}\frac{aV_T w - r_S i_P}{r_{SH} i_P - aV_T w} << r_{\text{pv}}\big|_{SC}. \tag{22}$$

TABLE I
DYNAMIC RESISTANCE [Ω] OF SEVERAL COMMERCIAL MODULES AT STC [34]

Module	OC	MPP	SC
REC-AE220	0.47	3.73	608
KC-200GT	0.22	3.46	415
IS-160	0.58	1.87	234
CNPV-280P	0.3	4.86	310
SF-160-24-M175	0.51	7.41	734

Table I presents the OC, SC and MPP PVG dynamic resistance values of several commercial solar modules at STC [3], well-supporting both (22) and the characteristics shown in Fig. 2.

V. PERTURBATION FREQUENCY DESIGN

In this Section, settling time T_Δ is derived for OC, MPP and SC conditions to reveal the highest value, based on which perturbation period should be selected. Boost power stage (cf. Fig. 7, where simplified control system, measurement interface and parameter values utilized in the experimental prototype are also given) often utilized as IPC, has been used in this paper. Nevertheless, information given in the subsequent section is equally applicable to other converters operating under single-loop MPPT control structure.

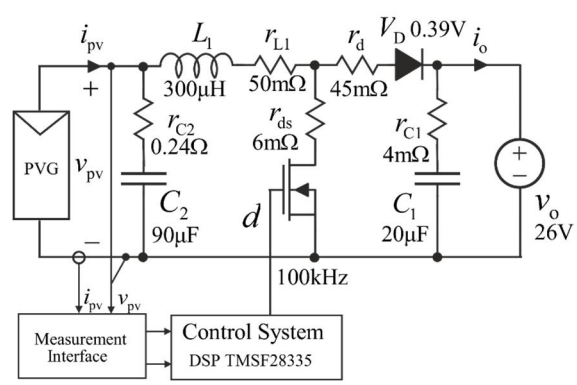

Fig. 7. Schematics of boost power stage based solar energy conversion system.

0278-0046 (c) 2016 IEEE. Personal use is permitted, but republication/redistribution requires IEEE permission. See http://www.ieee.org/publications_standards/publications/rights/index.html for more information.

This article has been accepted for publication in a future issue of this journal, but has not been fully edited. Content may change prior to final publication. Citation information: DOI 10.1109/TIE.2017.2674589, IEEE Transactions on Industrial Electronics

Dynamic modeling of the boost power stage in Fig. 7 was revealed in detail in [15]. The control-to-input-voltage transfer function of the IPC without PVG connected is given by (7) with

$$V_{\mathrm{DC}} = \frac{V_{\mathrm{e}} r_{\mathrm{pv}}}{r_{\mathrm{pv}} + R_{\mathrm{e}} - r_{\mathrm{C2}}}, \omega_{\mathrm{n}}^2 = \frac{r_{\mathrm{pv}} + R_{\mathrm{e}} - r_{\mathrm{C2}}}{L_1 C_2 (r_{\mathrm{pv}} + r_{\mathrm{C2}})}, \omega_{\text{z-esr}} = \frac{1}{r_{\mathrm{C2}} C_2}$$
$$\zeta_{\mathrm{pv}} = \frac{L_1 + C_2 \left(R_{\mathrm{e}} r_{\mathrm{pv}} + r_{\mathrm{C2}} (R_{\mathrm{e}} - r_{\mathrm{C2}}) \right)}{2\sqrt{\left(L_1 C_2 (r_{\mathrm{pv}} + r_{\mathrm{C2}}) \right) \left(r_{\mathrm{pv}} + R_{\mathrm{e}} - r_{\mathrm{C2}} \right)}}. \tag{23a}$$

and

$$V_{\mathrm{e}} = V_{\mathrm{o}} + V_{\mathrm{D}} + (r_{\mathrm{d}} - r_{\mathrm{ds}}) I_{\mathrm{pv}},$$
$$R_{\mathrm{e}} = r_{\mathrm{L1}} + r_{\mathrm{C2}} + D r_{\mathrm{ds}} + (1 - D) r_{\mathrm{d}}. \tag{23b}$$

According to (23), the converter exhibits underdamped behavior during transients [16], [17]. Assuming $r_{\mathrm{pv}} >> r_{\mathrm{C2}}$ and $r_{\mathrm{pv}} >> R_{\mathrm{e}}$, damping factor and natural frequency may further be simplified as

$$\zeta_{\mathrm{pv}} \approx \frac{1}{2}\left(\frac{1}{r_{\mathrm{pv}}} \sqrt{\frac{L_1}{C_2}} + R_{\mathrm{e}} \sqrt{\frac{C_2}{L_1}} \right), \ \omega_{\mathrm{n}}^2 \approx \frac{1}{L_1 C_2} \tag{24}$$

respectively, i.e. while the natural frequency is nearly independent of PVG dynamic resistance, the latter significantly influences the damping factor. Following (11) and taking into account (23) - (26), damping factor satisfies

$$\zeta_{\mathrm{pv,min}} < \zeta_{\mathrm{pv}} = \frac{1}{2}\left(\frac{1}{r_{\mathrm{pv}}} \sqrt{\frac{L_1}{C_2}} + R_{\mathrm{e}} \sqrt{\frac{C_2}{L_1}} \right) < \zeta_{\mathrm{pv,max}} \tag{25}$$

with

$$\zeta_{\mathrm{pv,min}} = \zeta_{\mathrm{pv}}\big|_{SC} = \frac{1}{2}\left(\frac{1}{r_{SH}} \sqrt{\frac{L_1}{C_2}} + R_{\mathrm{e}} \sqrt{\frac{C_2}{L_1}} \right) \approx \frac{R_{\mathrm{e}}}{2} \sqrt{\frac{C_2}{L_1}},$$
$$\zeta_{\mathrm{pv,max}} = \zeta_{\mathrm{pv}}\big|_{OC} = \frac{1}{2}\left(\frac{1}{r_S} \sqrt{\frac{L_1}{C_2}} + R_{\mathrm{e}} \sqrt{\frac{C_2}{L_1}} \right) \approx \frac{1}{2 r_S} \sqrt{\frac{L_1}{C_2}}. \tag{26}$$

Following (15a), settling time expressions are similar in CVR and CCR. Normalized settling time ($T_\Delta \omega_{\mathrm{n}}^{-1}$) dependence on the damping factor is shown in Fig. 8 for Δ = 0.1. Apparently, settling time increases monotonically with the decrease of ζ_{pv}, hence $T_\Delta\big|_{OC} < T_\Delta\big|_{SC}$ since $\zeta_{\mathrm{pv}}\big|_{SC} < \zeta_{\mathrm{pv}}\big|_{OC}$ (i.e. at OC condition, the shortest settling time would be expected).

In order to compare settling times at MPP and SC conditions, it is assumed that $\zeta_{\mathrm{pv}} << 1$ in both regions (rather practical assumption). Applying the approximation $\ln(1-x)\big|_{x<<1} \approx -x$ to (15), there is

$$T_\Delta \omega_{\mathrm{n}} \approx -\frac{\ln(\Delta)}{\zeta_{\mathrm{pv}}} \tag{27a}$$

in CCR and

$$T_\Delta \omega_{\mathrm{n}} \approx -\frac{\ln\left(\frac{\Delta}{2}\right)}{\zeta_{\mathrm{pv}}} \tag{27b}$$

in CPR. The CCR/CPR settling time ratio is then

$$\frac{T_\Delta\big|_{CCR}}{T_\Delta\big|_{CPR}} = \frac{k_\Delta \zeta_{\mathrm{pv}}\big|_{CPR}}{\zeta_{\mathrm{pv}}\big|_{CCR}} \tag{28}$$

with $k_\Delta = \ln(\Delta) \Big/ \ln\left(\frac{\Delta}{2}\right)$. Hence, in case $k_\Delta \zeta_{\mathrm{pv}}\big|_{CPR} > \zeta_{\mathrm{pv}}\big|_{CCR}$, settling time in CCR would be higher than in CPR. In classical control theory, 0.02 < Δ < 0.1 is typically used, corresponding to 0.77 < k_Δ < 0.85. On the other hand, the worst case CPR/CCR damping factor ratio is given by

$$\frac{\zeta_{\mathrm{pv}}\big|_{\mathrm{MPP}}}{\zeta_{\mathrm{pv}}\big|_{SC}} \approx \frac{\frac{1}{2 r_{\mathrm{pv}}\big|_{\mathrm{MPP}}} \sqrt{\frac{L_1}{C_2}} + \frac{R_{\mathrm{e}}}{2} \sqrt{\frac{C_2}{L_1}}}{\frac{R_{\mathrm{e}}}{2} \sqrt{\frac{C_2}{L_1}}} = 1 + \frac{1}{R_{\mathrm{e}} r_{\mathrm{pv}}\big|_{\mathrm{MPP}}} \frac{L_1}{C_2}. \tag{29}$$

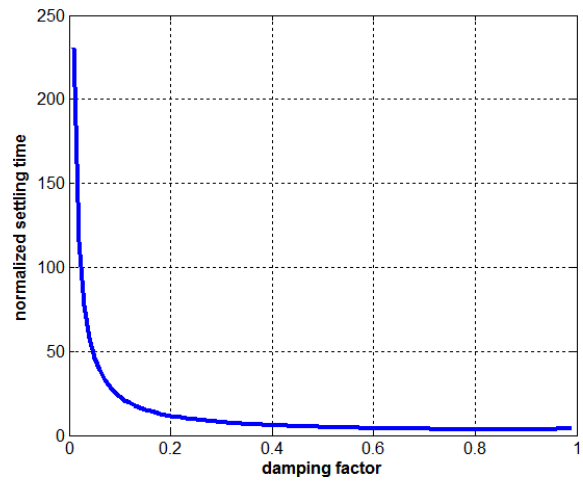

Fig. 8. Normalized settling time versus damping factor in CCR and CVR.

The second term on the right-hand side of (29) is typically much greater than unity since $R_{\mathrm{e}} r_{\mathrm{pv}}\big|_{\mathrm{MPP}} << 1$. Combining (27) and (29), it may be stated that in practical systems $T_\Delta\big|_{CCR} > T_\Delta\big|_{CPR}$ holds. Consequently, time interval ΔT between two consecutive perturbation instants must be selected so that

$$\Delta T > T_\Delta\big|_{SC} = -\frac{1}{\zeta_{\mathrm{pv}}\big|_{SC} \omega_{\mathrm{n}}} \ln\left(\Delta \sqrt{1 - \zeta_{\mathrm{pv}}^2\big|_{SC}} \right). \tag{30}$$

Moreover, according to $\zeta_{\mathrm{pv}}\big|_{SC}$ definition in (26), in case the value of r_{SH} is unknown, it may be assumed to be high enough to allow using $\zeta_{\mathrm{pv}}\big|_{SC} \approx \frac{R_{\mathrm{e}}}{2} \sqrt{\frac{C_2}{L_1}}$, which is totally independent of the PVG and relies only on IPC component values.

VI. Validation

In order to validate the presented material, experimental shown in Fig. 7 was put together. Raloss SR30-36 PV module composed of 36 series-connected monocrystalline silicon cells was used as the PVG. The module was illuminated by fluorescent lamps, capable of producing maximum irradiance of 500W/m^2, yielding short-circuit current of 1A and open-circuit voltage of 19.2V at 45°C panel temperature. Under

0278-0046 (c) 2016 IEEE. Personal use is permitted, but republication/redistribution requires IEEE permission. See http://www.ieee.org/publications_standards/publications/rights/index.html for more information.

This article has been accepted for publication in a future issue of this journal, but has not been fully edited. Content may change prior to final publication. Citation information: DOI 10.1109/TIE.2017.2674589, IEEE Transactions on Industrial Electronics

these conditions, $r_{SH} \approx 1000\Omega$ and $r_S \approx 0.91\Omega$. Detailed characterization of the PV panel can be found in [13]. The boost power stage operating as IPC was terminated by a 24V, 7.2Ah valve-regulated lead-acid battery. Croma 63103A electronic load was connected in parallel with the battery to maintain constant v_o = 26V during experiments by absorbing PVG generated power.

The system was first simulated using PSIM software. During the simulation, the converter duty cycle was swept from 0.7 down to 0.25 in steps of -0.03. Resulting PVG power, voltage and current are shown in Fig. 9. Apparently, settling time decreases along with the duty cycle since the operating point moves from CCR (t < 0.05) to CPR (0.05 < t < 0.06) and then to CVR (t > 0.06), as predicted by the presented theory. The existence of CPR is also well-supported by the simulations.

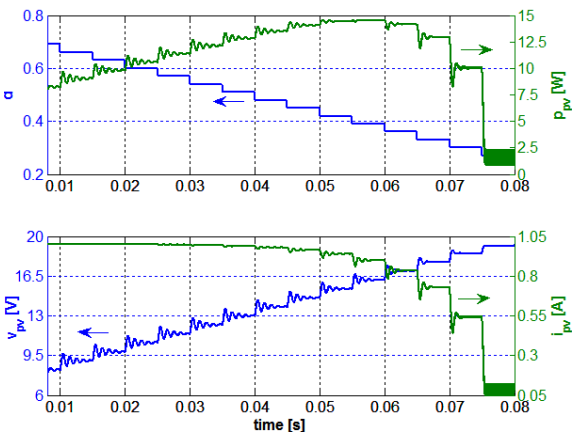

Fig. 9. Simulation results.

Measured P-V curve as well as dynamic and static resistances of the utilized PVG are shown in Figs. 10 and 11, respectively, with zoomed CPR region values. Note that $r_{pv}\big|_{SC} \approx 58 r_{pv}\big|_{MPP}$, justifying the assumptions made in the preceding Section.

During experiments, PVG power transient behavior was analyzed in the three subsequent operating points: (I_{pv}, V_{pv}) = (1A, 10V) in CCR, (I_{pv}, V_{pv}) = (0.91A, 16V) in CPR and (I_{pv}, V_{pv}) = (0.61A, 18V) in CVR. Corresponding values of the PVG dynamic resistance at the above operating points were measured as follows: r_{pv} = 285Ω in CCR, r_{pv} = 17.4Ω in CPR and r_{pv} = 3.8Ω in CVR. Fig. 12 presents measured PVG power, voltage and current responses in different operation regions to a step change in duty cycle. All the quantities are normalized to their steady-state values in order to highlight the variables relation during transients.

Fig. 12 explicitly demonstrates that measured PVG power transients behavior matches the analysis carried out in Section II based on the behavior of r_{pv} in different operational regions. In CCR, settling of the PVG power transient follows that of the PVG voltage and its duration is longest among different regions. In CPR, the PVG power transient is minimized due to the opposite settling behaviors of the PV voltage and current. In CVR, the PVG power transient settling behavior follows that of the PVG current, which is also much more damped compared to the settling behavior in CCR.

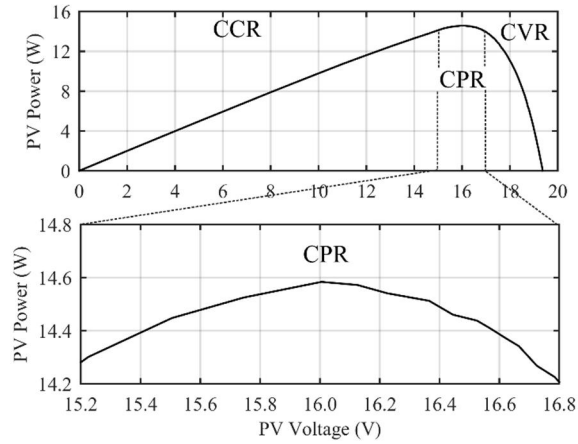

Fig. 10. Measured P-V curve of Raloss SR30-36 PV module.

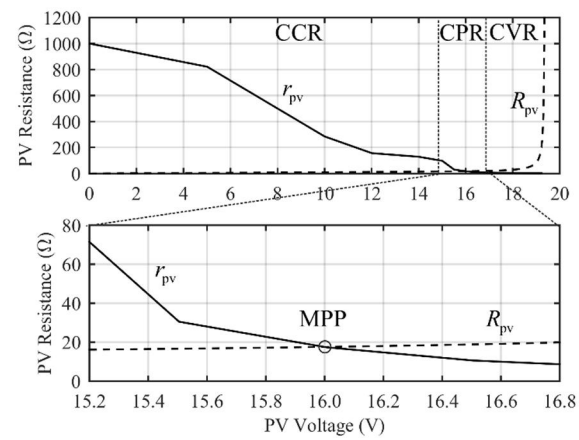

Fig. 11. Measured static and dynamic resistances of Raloss SR30-36 PV module.

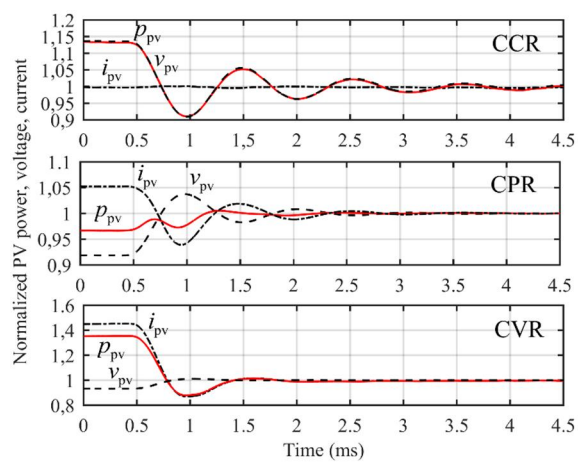

Fig. 12. Measured response of PVG power, voltage, and current to a step change in the IPC duty cycle.

According to the component values in Fig. 7, the values of r_{pv} stated above and the definition given in (27), damping factor is 0.0883 in CCR, 0.1925 at MPP, and 0.3286 in CVR while the undamped natural frequency is $\omega_n \approx 5.92 \cdot 10^3$rad/s. Hence, settling times are analytically obtained as 5.6ms in CCR, 3.3ms in CPR and 1.5ms in CVR for Δ = 0.05. Actual settling times are slightly lower because of unmodeled parasitic circuit resistances (i.e. actual dampings are higher than the predicted ones); nevertheless the fact that CCR

0278-0046 (c) 2016 IEEE. Personal use is permitted, but republication/redistribution requires IEEE permission. See http://www.ieee.org/publications_standards/publications/rights/index.html for more information.

This article has been accepted for publication in a future issue of this journal, but has not been fully edited. Content may change prior to final publication. Citation information: DOI 10.1109/TIE.2017.2674589, IEEE Transactions on Industrial Electronics

settling time is the longest among the three regions is well evident.

Once the perturbation frequency has been set, perturbation step size should be determined. P&O algorithm can be confused and track the MPP in wrong direction when power variation caused by irradiation change (ΔP_G) is larger than that ((ΔP_v) induced during MPPT algorithm perturbation interval [2,18-20]. Therefore,

$$\left|\Delta P_{\mathrm{v}}\right| > \left|\Delta P_{\mathrm{G}}\right| \tag{33}$$

must be satisfied for all atmospheric conditions [21]. Moreover, perturbation step size must be designed in CPR, since $\Delta P_{\mathrm{pv}}^{CPR} << \Delta P_{\mathrm{pv}}^{CVR}$ and $\Delta P_{\mathrm{pv}}^{CPR} << \Delta P_{\mathrm{pv}}^{CCR}$, see (12). The authors of [2] have used second-order Taylor approximation for the P-V curve in the vicinity of the MPP. Based on this method, one can estimate the smallest duty cycle perturbation $\Delta d_{\min}$, satisfying (32). In the estimation, the following parameters are used: material constant K_{ph} = 1.9mA, saturation current I_s = 1.097·10^{-10}A and ideality factor η = 1.0. These parameters yield $\Delta d_{\min}$ = 0.0178, producing power variation capable to overcome that caused by irradiation ramp of 100W/m^2/s within the interval of 5.6ms. Nevertheless, in addition to irradiation variations, finite resolution of utilized analog-digital converter (ADC) should also be taken into account [21]. Texas Instruments' TMS320F28335 Digital Signal Processor utilizes 12-bit ADC with 3-V full-scale voltage span (i.e. ADC resolution is 0.37 mV). Taking into account the ADC quantization error of [21], minimum duty cycle perturbation step size will becomes $\Delta d_{\min}$ = 0.0206.

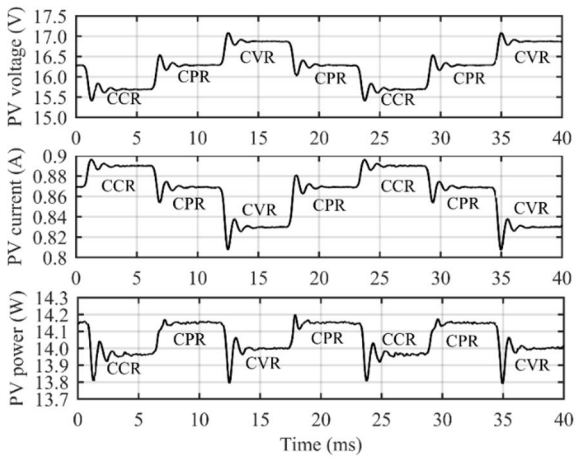

Fig. 13. Measured PVG voltage, current, and power during steady-state MPPT process under non-varying atmospheric conditions.

Fig. 13 presents measured waveforms of steady-state MPP-tracking process, utilizing the above calculated perturbation frequency and duty cycle step size (i.e., 1/5.6 kHz and 0.0206, respectively). The behavior of the PVG power, voltage, and current clearly demonstrates that the operating point oscillates within a region (rather than resting) even under non-varying atmospheric conditions. Settling behavior of PVG power depends on operating point location, as predicted. Therefore, perturbation frequency design should be accomplished assuming the worst case CCR operating point to ensure correct operation of direct MPPT algorithms.

VII. Conclusions

Photovoltaic generator characteristic curve is usually split into constant current and constant voltage regions, connected by the maximum power point. Detailed analysis of photovoltaic generators P-V curve shape and power transient behavior carried out in the paper revealed that exact maximum power point does not exist in practice due to finite resolution of measuring facility. Instead, steady state operating point may reside within a region (referred to as constant power region) around the maximum power point. Thus, during maximum power point tracking process, the operating point may reside in any of the three regions even under constant atmospheric conditions. Moreover, photovoltaic generator power transient settling process was shown to behave differently in the three regions. The longest settling time was exposed to take place in the constant current region, where the damping of the combined system is the lowest. Consequently, unlike stated in design guidelines utilized so far, perturbation frequency design of direct maximum power point tracking algorithms must be accomplished for the worst-case operating point expected in the constant current region (rather than in maximum power point, as proposed by the existing design guidelines). Moreover, once short-circuit conditions are assumed as the worst-case possible operating point, it was revealed that photovoltaic generator influence on perturbation frequency value vanishes and the latter may be carried out based on interfacing converter component values only. The revealed findings were successfully verified by means of simulations and experiments.

References

[1] S. Lyden and M. E. Haque, "Maximum power point tracking techniques for photovoltaic systems: A comprehensive review and comparative analysis," *Renew. Sust. Energy Rev.*, vol. 52, pp. 1504-1518, 2015.

[2] N. Femia, G. Petrone, G. Spagnuolo, and M. Vitelli, "Optimization of perturb and observe maximum power point tracking method," *IEEE Trans. Power Electron.*, vol. 20, no. 4, pp. 963-973, Jul. 2005.

[3] P. Manganiello, M. Ricco, G. Petrone, E. Monmasson, and G. Spagnuolo, "Dual-Kalman-filter-based identification and real-time optimization of PV systems," *IEEE Trans. Ind. Electron.*, vol. 62, no. 11, pp. 7266-7275, Nov. 2015.

[4] P. Manganiello, M. Ricco, G. Petrone, E. Monmasson, and G. Spagnuolo, "Optimization of perturbative PV MPPT methods through on line system identification," *IEEE Trans. Ind. Electron.*, vol. 61, no. 12, pp. 6812-6821, Dec. 2014.

[5] A. Ahmed, L. Ran, S. Moon, and J.-H, Park, "A fast PV power tracking control algorithm with reduced power mode," *IEEE Trans. Energy Convers.*, vol. 28, no. 3, pp. 565-575, Sep. 2013.

[6] A. Sangwongwanich, Y. Yang, and F. Blaabjerg, "High-performance constant power generation in grid-connected PV systems," *IEEE Trans. Power Electron.*, vol. 31, no. 3, pp. 1822-1825, Mar. 2016.

[7] Y. Yang, H. Wang, F. Blaabjerg, and T. Kerekes, "Hybrid power control concept for PV inverters with reduced thermal loading," *IEEE Trans. Power Electron.*, vol. 29, no. 12, pp. 6271-6275.

[8] R. Tonkoski, L. A. C. Lopes, and T. H. M. El-Fouly, "Coordinated active power curtailment of grid connected PV inverters for overvoltage prevention," *IEEE Trans. Sust. Energy*, vol. 2, no. 2, pp. 139-147, Apr. 2011.

[9] S. Liu and R. A. Dougal, "Dynamic multiphysics model for solar array," *IEEE Trans. Energy Convers.*, vol. 17, no. 2, pp. 285-294, Jun. 2002.

[10] L. Nousiainen, et al., "Photovoltaic generator as an input source for power electronic converters," *IEEE Trans. Power Electron.*, vol. 28, no. 6, pp. 3028-3028, Jun. 2013.

[11] W. Xiao, W. G. Dunford, P. R. Palmer, and A. Capel, "Regulation of photovoltaic voltage," *IEEE Trans. Ind. Electron.*, vol. 54, no. 3, pp. 1365-1374, Jun. 2007.

0278-0046 (c) 2016 IEEE. Personal use is permitted, but republication/redistribution requires IEEE permission. See http://www.ieee.org/publications_standards/publications/rights/index.html for more information.

This article has been accepted for publication in a future issue of this journal, but has not been fully edited. Content may change prior to final publication. Citation information: DOI 10.1109/TIE.2017.2674589, IEEE Transactions on Industrial Electronics

[12] T. Esram, J. W. Kimball, P. T. Krein, P. L. Chapman, and P. Midya, "Dynamic maximum power point tracking of photovoltaic arrays using ripple correlation control," *IEEE Trans. Power Electron.*, vol. 21, no. 5, pp. 1282-1291, Sept. 2006.

[13] T. Suntio, J. Leppäaho, J. Huusari, and L. Nousiainen, "Issues on solar-generator-interfacing with current-fed MPP-tracking converters," *IEEE Trans. Power Electron.*, vol. 25, no. 9, pp. 2409-2419, Sep. 2010.

[14] J. L. Wyatt and L. O. Chua, "Nonlinear resistive maximum power theorem with solar cell application," *IEEE Trans. Circuits. Syst.*, vol. Cas-30, no. 11, pp. 824-828, Nov. 1983.

[15] J. Viinamäki, J. Jokipii, T. Messo, M. Sitbon, and A. Kuperman, "Comprehensive dynamic analysis of PV-generator-interfacing DC-DC boost-power-stage converter," *IET Renew. Power Gen.*, vol. 9, no. 4, pp. 306-314, Apr. 2015.

[16] E. Romero-Cadaval, G. Spagnuolo, L. Franquelo, et al., "Grid-connected photovoltaic generation plants – Components and operation," *IEEE Ind. Electron. Mag.*, vol. 7, no. 3, pp. 6-20, Sep. 2013.

[17] K. Ogata, *Modern Control Engineering*, Upper Saddle River, NJ, USA; Prentice-Hall, 1997.

[18] K. Hussein, I. Muta, T. Oshino, and M. Osaka, "Maximum photovoltaic power tracking: an algorithm for rapidly changing atmospheric conditions," *IEE Proc. – Gen. Trans. Dist.*, vol. 142, no. 1, pp. 59-64, Jan. 1995.

[19] D. Sera, R. Teodorescu, J. Hantschel, and M. Knoll, "Optimized maximum power point tracker for fast-changing environmental conditions," *IEEE Trans. Ind. Electron.*, vol. 55, no. 7, pp. 2629-2637, Jul. 2008.

[20] S. Kjær, "Evaluation of the "Hill Climbing" and the "Incremental Conductance" maximum power point trackers for photovoltaic power systems," *IEEE Trans. Energy Convers.*, vol. 27, no. 4, pp. 922-929, Dec. 2012.

[21] N. Femia, G. Petrone, G. Spagnuolo, and M. Vitelli, *Power Electronics and Control Techniques for Maximum Power Harvesting in Photovoltaic Systems*, Boca Raton, FL, USA; CRC Press, 2013.

[22] S. Kolesnik, M. Sitbon, S. Gadelovits, T. Suntio and A. Kuperman, "Interfacing renewable energy sources for maximum power transfer - Part II: Dynamics," *Renew. Sust. Energy Rev.*, vol. 51, pp. 1771 – 1783, 2015.

[23] M. Sitbon, J. Leppaaho, T. Suntio and A. Kuperman, "Dynamics of photovoltaic generator interfacing voltage controlled buck power stage," *IEEE J. Photovolt.*, vol. 5, no. 2, pp. 633 – 640, Mar. 2015.

[24] M. Sitbon, S. Schacham and A. Kuperman, "Disturbance observer based voltage regulation of current-mode-boost-converter-interfaced photovoltaic generator," *IEEE Trans. Ind. Electron.*, vol. 62, no. 9, pp. 5776 – 5785, Sep. 2015.

[25] M. A. Elgendy, B. Zahavi and D. J. Atkinson, "Assessment of perturb and observe MPPT algorithm implementation techniques for PV pumping applications," *IEEE Trans. Sust. Energy*, vol. 3, no.1, pp. 21-33, Jan. 2012.

[26] M. A. Elgendy, B. Zahavi and D. J. Atkinson, "Assessment of incremental conductance maximum power point tracking algorithm," *IEEE Trans. Sust. Energy*, vol. 4, no. 1, pp. 108-117, Jan. 2013.

[27] S. Lineykin, M. Averbukh and A. Kuperman, "Issues in modeling amorphous silicon photovoltaic modules by single-diode equivalent circuit," *IEEE Trans. Ind. Electron.*, vol. 61, no. 12, pp. 6785 – 6793, Dec. 2014.

[28] Y. Mahmoud and E. El-Saadany, "A photovoltaic model with reduced computational time," *IEEE Trans. Ind. Electron.*, vol. 62, no. 6, pp. 3534 – 3544, Jun. 2015.

[29] E. Batzelis and S. Papathanassiou, "A method for the analytical extraction of the single-diode PV model parameters," *IEEE Trans. Sust. Energy*, vol. 7, no. 2, pp. 504 – 512, Apr. 2016.

[30] S. Lineykin, M. Averbukh and A. Kuperman, "An improved approach to extracting the single-diode equivalent circuit parameters of a photovoltaic cell/panel," *Renew. Sust. Energy Rev.*, vol. 30, pp. 282 – 289, 2014.

[31] E. Batzelis, G. Kampitsis, S. Papathanassiou and S. Manias, "Direct MPP calculation in terms of the single-diode PV model parameters," *IEEE Trans. Energy Convers.*, vol. 30, no. 1, pp. 226 – 236, Mar. 2015.

[32] A. Kuperman, S. Lineykin, V. Lo Brano, G. Ciulla and T. Suntio, "Obtaining dynamic Norton parameters of a solar panel from manufacturer data," in Proc. *Power Electron. Mach. Drives (PEMD'16) Conf.*, Apr. 19-21, Glasgow, UK, 2016.

[33] G. Farivar, B. Asaei and S. Mahrnami, "An analytical solution for tracking photovoltaic module MPP," *IEEE J. Photovolt.*, vol. 3, no. 3, pp. 1053 – 1061, Jul. 2013.

[34] A. Kuperman, "Comments on 'An analytical solution for tracking photovoltaic module MPP'," *IEEE J. Photovolt.*, vol. 4, no. 2, pp. 734 – 735, Mar. 2014.

[35] M. A. Elgendy, D. J. Atkinson and B. Zahavi, "Experimental investigation of the incremental conductance maximum power point tracking algorithm at high perturbation rates," *IET Renew. Power Gen.*, vol. 10, no.2, pp. 133-139, 2016.

[36] M. A. Elgendy, B. Zahavi and D. J. Atkinson, "Operating characteristics of the P&O algorithm at high perturbation frequencies for standalone PV systems," *IEEE Trans. Energy Convers.*, vol. 30, no.1, pp. 189-198, Mar. 2015.

[37] R.W. Erikson and D. Maksimovic. *Fundamentals of power electronics*, 2nd ed. Kluwer Academic Publishers, Norwell, MA.

0278-0046 (c) 2016 IEEE. Personal use is permitted, but republication/redistribution requires IEEE permission. See http://www.ieee.org/publications_standards/publications/rights/index.html for more information.